

## FAST drift scan survey for H<sub>I</sub> intensity mapping: II. stacking-based primary beam construction for FAST L-band 19 feeds at 1.4 GHz

XINYANG ZHAO <sup>1</sup>, YICHAO LI <sup>1</sup>, WENXIU YANG <sup>2,3,4</sup>, FUREN DENG <sup>2,3,4,5</sup>, YOUANG WANG <sup>2,4,3,1</sup>, FENGQUAN WU <sup>2,3,4</sup>,  
XIN WANG <sup>6,7</sup>, XIAOHUI SUN <sup>8</sup>, XIN ZHANG <sup>1,9,10</sup> AND XUELEI CHEN <sup>2,1,4,3</sup>

<sup>1</sup>Liaoning Key Laboratory of Cosmology and Astrophysics, College of Sciences, Northeastern University, Shenyang 110819, China

<sup>2</sup>National Astronomical Observatories, Chinese Academy of Sciences, Beijing 100101, China

<sup>3</sup>School of Astronomy and Space Science, University of Chinese Academy of Sciences, Beijing 100049, China

<sup>4</sup>Key Laboratory of Radio Astronomy and Technology, Chinese Academy of Sciences, A20 Datun Road, Chaoyang District, Beijing 100101, China

<sup>5</sup>Institute of Astronomy, University of Cambridge, Madingley Road, Cambridge, CB3 0HA, UK

<sup>6</sup>School of Physics and Astronomy, Sun Yat-Sen University, No. 2 Daxue Rd., Zhuhai 519082, People's Republic of China

<sup>7</sup>CSST Science Center for the Guangdong–Hong Kong–Macau Greater Bay Area, SYSU, People's Republic of China

<sup>8</sup>School of Physics and Astronomy, Yunnan University, Kunming, 650091, P. R. China

<sup>9</sup>National Frontiers Science Center for Industrial Intelligence and Systems Optimization, Northeastern University, Shenyang 110819, China

<sup>10</sup>Key Laboratory of Data Analytics and Optimization for Smart Industry (Ministry of Education), Northeastern University, Shenyang 110819, China

### ABSTRACT

Neutral hydrogen (H<sub>I</sub>) intensity mapping (IM) presents great promise for future cosmological large-scale structure surveys. However, a major challenge for H<sub>I</sub> IM cosmological studies is to accurately subtract the foreground contamination. An accurate beam model is crucial for improving foreground subtraction accuracy. In this work, we develop a stacking-based beam reconstruction method utilizing the radio continuum point sources within the drift-scan field. Based on the Five-hundred-meter Aperture Spherical radio Telescope (FAST), we employ two series of drift-scan survey data and merge the measurements to construct the beam patterns of the FAST L-band 19 feeds. To model the beams, we utilize the Zernike polynomial (ZP), which effectively captures asymmetric features of the main beam and the different side lobes. Due to the symmetric location of the beams, the main features of the beams are closely related to the distance from the center of the feed array, e.g., as the distance increases, side lobes become more pronounced. This modeling pipeline leverages the stable drift-scan data to extract beam patterns exclude the reflector's changing effects, and provides a more accurate measurement beam and a more precise model beam for FAST H<sub>I</sub> IM cosmology surveys.

**Keywords:** Large-scale structure of the universe (902) — Astronomical methods (1043) — Radio astronomy (1338) — Surveys (1671) – Drift scan imaging (410)

### 1. INTRODUCTION

Neutral hydrogen intensity mapping (H<sub>I</sub> IM), which is to measure the total H<sub>I</sub> intensity of many galaxies within large voxels (e.g. Battye et al. 2004; McQuinn et al. 2006), has been proposed as a novel method for cosmic large-scale structure surveys in the epoch of post-reionization (Chang et al. 2008; Loeb & Wyithe 2008; Mao et al. 2008; Pritchard & Loeb 2008; Wyithe & Loeb 2008; Wyithe et al. 2008; Peterson et al. 2009; Bagla et al. 2010; Seo et al. 2010; Lidz et al. 2011; Ansari et al. 2012; Pritchard & Loeb 2012; Battye et al. 2013).

It can be rapidly conducted and expanded to cover substantial survey areas, making it well-suited for cosmological surveys (Xu et al. 2015; Jin et al. 2020; Zhang et al. 2021; Jin et al. 2021; Wu & Zhang 2022; Wu et al. 2023b,a; Zhang et al. 2023; Pan et al. 2024).

The H<sub>I</sub> IM technique was investigated by measuring the cross-correlation function between an H<sub>I</sub> IM survey and an optical galaxy survey. Chang et al. (2010) for the first time reports the cross-correlation function detection using the H<sub>I</sub> IM carried out with Green Bank Telescope (GBT) and an optical galaxy survey. Later, several detections of the cross-correlation power spectrum between an H<sub>I</sub> IM survey and an optical galaxy survey were reported (Masui et al. 2013; Anderson et al. 2018; Wolz et al. 2017, 2022; Amiri et al. 2023).

Recently, the MeerKAT H<sub>I</sub> IM survey (Bull et al. 2015; Cunningham et al. 2021; Li et al. 2021; Wang et al. 2021; Paul et al. 2021; Chen et al. 2023) reported the cross-correlation power spectrum detection with the optical galaxy survey (Cunnington et al. 2023). Meanwhile, the H<sub>I</sub> IM auto power spectrum on Mpc scales is detected using the MeerKAT interferometric observations (Paul et al. 2023). However, the H<sub>I</sub> IM auto power spectrum on large scales remains undetected (Switzer et al. 2013). Besides, several H<sub>I</sub> IM experiments are targeting the post-reionization epoch, with some currently collecting data, including projects like the Tianlai project <sup>1</sup> (Chen 2012; Li et al. 2020; Wu et al. 2021; Perdureau et al. 2022; Sun et al. 2022) and the Canadian Hydrogen Intensity Mapping Experiment (CHIME <sup>2</sup>; Bandura et al. 2014), while others are in the construction phase, such as the Baryonic Acoustic Oscillations from Integrated Neutral Gas Observations (BINGO <sup>3</sup>; Battye et al. 2013) and the Hydrogen Intensity and Real-time Analysis eXperiment (HIRAX <sup>4</sup>; Newburgh et al. 2016). The H<sub>I</sub> IM technique is also proposed as the key cosmology project with Square Kilometre Array (SKA <sup>5</sup>; Santos et al. 2015; Square Kilometre Array Cosmology Science Working Group et al. 2020). With the Five-hundred-meter Aperture Spherical radio Telescope, (FAST; Nan et al. 2011; Li & Pan 2016) H<sub>I</sub> IM survey shows considerable potential for cosmological studies (Li & Ma 2017; Hu et al. 2020).

The major challenge for H<sub>I</sub> IM cosmology studies is to separate the H<sub>I</sub> brightness fluctuation from the foreground contamination, i.e. the synchrotron or free-free emission of the Milky Way and radio galaxies, which are typically several orders of magnitude brighter than the cosmological signal (Wolz et al. 2015; Spinelli et al. 2022). Exploiting the advantageous characteristic of foreground contamination exhibiting smoothness across the frequency spectrum, it becomes feasible to be separated from the fluctuating HI signal (Bowman et al. 2009; Ansari et al. 2012). However, systematic effects exist during the observation significantly increase the degree of freedom of the foreground frequency spectrum and challenges the foreground separation technique (Matshawule et al. 2021; Spinelli et al. 2022; Irfan et al. 2024). The primary beam effect is one of the significant systematic effects that must be taken into account while analyzing the H<sub>I</sub> IM survey data.

The primary beam effect refers to two important aspects of the antenna beam pattern. The first is the main lobe shape and its frequency dependence; the second is the side-lobe beam

pattern level and its frequency-dependent variation. Both can weaken the smooth foreground spectrum assumption, resulting in a failed foreground subtraction (Matshawule et al. 2021; Spinelli et al. 2022). To address such primary beam effects, the observed H<sub>I</sub> maps are usually degraded to a common beam size, i.e. the largest beam size within the observation bandwidth, with an assumption of simple Gaussian primary beam shape (Masui et al. 2013; Anderson et al. 2018; Cunningham et al. 2023). This approach can reduce the primary beam effect to a subdominant level while also significantly suppressing the signal-to-noise ratio. Recently, a deep-learning-based strategy has been developed with simulated data for reducing the H<sub>I</sub> IM survey systematic effect, which includes both the primary beam effect (Ni et al. 2022) and the polarization leakage effect (Gao et al. 2023). To apply such a strategy to the realistic observation data, an accurate beam model is required for training the deep learning network.

The beam pattern can be properly measured via radio holographic measurements with an interferometer (Iheanetu et al. 2019; Asad et al. 2021; Amiri et al. 2024), or by scanning a bright celestial calibrator for a single dish telescope (e.g. Jiang et al. 2020). Besides, the Tianlai experiment has measured the primary beam via unmanned aerial vehicle (Zhang et al. 2021) and CHIME has measured the primary beam via the sun transition (Amiri et al. 2022). The FAST beam pattern combines the response pattern of the coaxial feed and the reflector. The FAST L-band observation adopts a 19-feed array mounted in the focus cabin suspended on the cables about the reflector. The reflector consists of about 4 400 active reflector panels, which form a 300 m paraboloid at each pointing direction. Such a complicated reflector and feed arrangement heavily increases beam pattern instabilities, resulting in a direction-dependent beam pattern (Dong & Han 2013). In this work, we developed a stacking-based beam pattern construction method employing H<sub>I</sub> IM drift scan observation data itself. Because the beam shape is measured in the same direction as the H<sub>I</sub> IM survey observation, we may minimize the direction dependency impact and achieve the beam pattern that is close to the actual case during the observation.

The rest of the paper is organized as follows: Section 2 introduces the datasets used in this work. In Section 3, we describe the detailed stacking-based beam pattern reconstruction method. The results and discussion are presented in Section 4, followed by our conclusions in Section 5.

## 2. DATA AND PREPROCESSING

### 2.1. FATHOMER

We employ the drift scan observation data from the FAST neuTRal HyDrOgen intensity Mapping ExPeRiment (FATHOMER; Li et al. 2023). In this analysis,  $18 \times 4$  hr drift scan observation data with integration time of 1 s per times-

<sup>1</sup> <https://tianlai.bao.ac.cn>

<sup>2</sup> <https://chime-experiment.ca/en>

<sup>3</sup> <https://bingotelescope.org>

<sup>4</sup> <https://hirax.ukzn.ac.za>

<sup>5</sup> <https://www.skao.int>

**Table 1.** The observational data used in this work. In these observations, the low-level noise diode is adopted and the feed array is rotated by  $23.4'$  during each observation.

FATHOMER <sup>†</sup>		CRAFTS <sup>‡</sup>	
Field center <sup>*</sup>	Date	Field center	Date
1100+2600	20210302	0330+2715	20220418
1100+2600	20220210	0330+2737	20201029
1100+2610	20210309	0330+2759	20201118
1100+2610	20210314	0330+2820	20201027
1100+2610	20220211	0330+2904	20200805
1100+2621	20210313	0330+2925	20200806
1100+2621	20220212	0330+2947	20200821
1100+2632	20210305	0330+3009	20200822
1100+2632	20220213	0330+3030	20200810
1100+2643	20210306	0330+3052	20200813
1100+2643	20220214	0330+3114	20200818
1100+2654	20210307	0330+3135	20220330
1100+2654	20220215	0330+3157	20220324
1100+2705	20220216	0330+3219	20220328
1100+2715	20220222		
1100+2726	20220217		
1100+2737	20220218		
1100+2748	20220219		

<sup>†</sup> The FATHOMER observations are carried out for 4 hours drift-scan every nights with 1 second integration time.

<sup>‡</sup> The CRAFTS observations are carried out for 5 hours drift-scan every nights with 0.2 second integration time.

<sup>\*</sup> The field center, encoded with 'HHMM+ddmm', indicates the center of each drift scan survey field, where 'HHMM' represents the R.A. and '+ddmm' represents the decl., respectively.

tamp are used, which targets the area that covers the R.A. range from 9 to 13 hr, overlapping with the Northern Galactic Cap (NCP) area of the Sloan Digital Sky Survey (SDSS; Reid et al. 2016). The drift scan time-ordered data are pre-processed via the analysis pipeline developed in Li et al. (2023). Following the pipeline, the full frequency band is first split into three sub-bands, i.e. the low-frequency band 1050–1150 MHz, the mid-frequency band 1150–1250 MHz, and the high-frequency band 1250–1450 MHz. In this work, we use the high-frequency band data as it is less contaminated by RFI. The high-frequency band also covers the continuum spectrum range of the celestial point source catalog, which is used as a sky model for beam pattern construction. Extending the lower frequency band requires a better knowledge of the source spectrum model. The selected data are then RFI flagged and flux calibrated before proceeding to the analysis of this work.

## 2.2. CRAFTS

The Commensal Radio Astronomy FasT Survey (CRAFTS; Li et al. 2018) is designed to cover the FAST sky between decl. of  $-14^\circ$  and  $+66^\circ$  and proposed to carry out multiple surveys

simultaneously in a single drift scan observation, including Galactic HI, extra-galactic HI, pulsar search, and transient surveys. This analysis uses  $14 \times 5$  hr CRAFTS drift scan observation data, which targets the area that covers the R.A. range from 1 to 6 hr and the decl. range from  $27^\circ 15'$  to  $32^\circ 19'$ . CRAFTS drift scan observation data have the high-cadence noise diode signal injection and the noise diode temperature was pre-calibrated (Jiang et al. 2020). The integration time for CRAFTS is 0.2 s per timestamp. We reduce the integration time to 1 s after the calibration processing. We adopt the same frequency partition strategy and time-ordered data analysis pipeline as the FATHOMS analysis. All the FAST drift scan data used in this work are summarized in Table 1.

## 2.3. NVSS

Our stacking-based beam construction requires a sky model, which is constructed using the continuum flux density measurements from the NRAO-VLA Sky Survey (NVSS) catalog (Kimball & Ivezić 2008). The integrated flux density of NVSS sources is extracted from the Unified Radio Catalog <sup>6</sup>, which is a combined radio objects catalog with the correction of the flux and position.

The FATHOMER and CRAFTS survey fields are both fully covered by the NVSS field. Both the FATHOMER and CRAFTS surveys adopt the drift scan observation mode, which is scanning at a constant decl. within an R.A. range. During the drift scans, the 19-feed array is rotated by  $23.4^\circ$  to obtain the optimized field coverage (Li et al. 2018). Therefore, the same sources might be observed multiple times by different feeds. In addition, we also selected the sources with their decl. within  $10'$  to the scanning decl. to recover a full pattern beyond the size of the main beam. We choose a total area of  $\sim 138 \text{ deg}^2$  and  $\sim 385 \text{ deg}^2$  NVSS field for FATHOMER and CRAFTS, respectively. The total numbers of sources within the survey areas are 7 463 and 21 015 for FATHOMER and CRAFTS, respectively. However, not all the sources are used in the beam pattern construction. Some of the sources are dropped because they are either poorly observed or highly contaminated by RFI or nearby sources. The detailed source selection criteria are presented in Section 3.3.

We select a frequency range between 1375 MHz–1425 MHz which is relatively RFI-free and central at the NVSS observation frequency. We also assume a smooth power-law spectrum for the sources and adopt the NVSS median spectral index of 0.7 (Condon et al. 1998) to calculate the flux density at each frequency. The NVSS sources are assumed to be unresolved point sources and their flux densities are then converted to brightness temperature assuming a constant gain factor, i.e. DPFU (Degree Per Flux Unit)  $A_{\text{eff}}/2k_B = 25.6 \text{ K Jy}^{-1}$  (Jiang et al. 2020).

<sup>6</sup> <http://www.aoc.nrao.edu/~akimball/radiocat.shtml>

### 3. METHOD

#### 3.1. Beam stacking

The time-ordered data is expressed as the combination of beam-convolved sky and noise,

$$\mathbf{d} = \mathbf{P}\mathbf{M}\mathbf{b} + \mathbf{n}, \quad (1)$$

where  $\mathbf{d}$  and  $\mathbf{n}$  are the time-ordered data vector and the noise vector, with the vector element representing the flux measurements and the corresponding noise at each time stamp, respectively. The multiplication of  $\mathbf{M}\mathbf{b}$  represents the convolution of the sky model and the beam kernel.  $\mathbf{b} = \{\mathbf{B}_0^T, \mathbf{B}_1^T, \dots, \mathbf{B}_q^T\}^T$  is a column vector by stacking the columns of beam matrix  $\mathbf{B}$  with size  $(q, q)$ , where  $\mathbf{B}_i$  represents the  $i$ -th column of the beam matrix. Matrix  $\mathbf{M}$  is a special matrix of size  $(p, q^2)$ , where  $p$  is the number of pixels within the survey area. the matrix  $\mathbf{M}$  captures the convolutional spatial relationships between the pixels of the sky and the beam kernel matrix  $\mathbf{B}$ , i.e. each row of the matrix  $\mathbf{M}$  is contracted by stacking the pixels covered by the beam kernel at each pointing direction. The matrix  $\mathbf{P}$  is the projection matrix that maps the beam-convolved sky pixels to the time stamps.

To get the estimation of the beam kernel  $\mathbf{b}$  in the presence of noise, the  $\chi^2$  is expressed as,

$$\chi^2 = (\mathbf{d} - \mathbf{P}\mathbf{M}\mathbf{b})^T \mathbf{C}_N^{-1} (\mathbf{d} - \mathbf{P}\mathbf{M}\mathbf{b}), \quad (2)$$

where  $\mathbf{C}_N = \langle \mathbf{n}\mathbf{n}^T \rangle$  is the noise covariance matrix. As shown in previous work (i.e. Li et al. 2023), the FAST drift scan observation exhibit stable noise level and the correlated noise is eliminated with the temporal gain calibration. To simplify the estimation, the noise covariance matrix is assumed to be an identity matrix. By minimizing  $\chi^2$ , the beam kernel estimator is expressed as,

$$\hat{\mathbf{b}} = \left( (\mathbf{P}\mathbf{M})^T \mathbf{C}_N^{-1} (\mathbf{P}\mathbf{M}) \right)^{-1} (\mathbf{P}\mathbf{M})^T \mathbf{C}_N^{-1} \mathbf{d}. \quad (3)$$

The beam matrix is then expressed as,

$$\hat{\mathbf{B}} = \{\hat{b}_{1,\dots,q}^T, \hat{b}_{q+1,\dots,2q}^T, \dots, \hat{b}_{q(q-1)+1,\dots,q^2}^T\}, \quad (4)$$

where  $\hat{b}_{i,\dots,j}$  represents a vector composed with the  $i$ -th to  $j$ -th elements of  $\hat{\mathbf{b}}$ .

In this work, the beam pattern is represented with a  $100 \times 100$  matrix, covering  $20'$  in both dimensions, which is large enough to include the first few side lobes.

#### 3.2. The sky model

The sky model is constructed with the continuum flux density of sources from the NVSS catalog. Because the FAST beam size is  $\sim 3'$ , all the NVSS sources are assumed to be unresolved and the sky model is expressed as,

$$m(\alpha, \beta) = \sum_{i=1}^{N_S} S_i \delta_{\alpha\alpha_i, \beta\beta_i}, \quad (5)$$

where  $\delta_{\alpha\alpha_i, \beta\beta_i}$  is the Kronecker delta function,  $m(\alpha, \beta)$  is the flux density of the map,  $(\alpha, \beta)$  represent the coordinate of the map pixel, i.e. R.A., and decl.,  $(\alpha_i, \beta_i)$  represents the coordinate of the  $i$ -th sources with flux density of  $S_i$ , and  $N_i$  is the total number of sources in the chosen area. We use all the sources with flux density over 20 mJy to construct the sky model.

#### 3.3. Source selection criteria

The matrix  $\mathbf{P}$  represents the projection between the maps and the time-ordered domains. Thus, it has the shape of  $t \times p$ , where  $p$  is the number of pixels of the sky model and  $t$  is the number of time stamps. Utilizing the complete time-ordered observational data yields a large  $\mathbf{P}$  matrix, rendering the subsequent matrix operation both time- and memory-intensive. On the other hand, not all the observational data are useful for beam measurements. For instance, the RFI-contaminated data are removed at the first stage of data selection. Although we chose a frequency band that is relatively RFI-free, there still are time stamps that are badly contaminated by transient objects, e.g. the navigation satellites. In addition, the sources with other sources around, are not the ideal calibrator for characterizing the beam pattern. Thus, we only chose the time-ordered data with bright isolated sources for the following beam stacking analysis, which significantly reduces the amount of observation data.

A straightforward isolating method is to remove the sources with any other sources within the radius of  $5'$ . We apply the straightforward isolating method to the initial NVSS catalog before applying the 20 mJy flux threshold. Such a straightforward isolating method significantly reduces the amount of observation data. However, it indiscriminately removes both the bright and dim sources.

To keep as many bright sources as possible, we consider a flux-weighted isolating method. We apply a point spread function (PSF) to each of the sources and calculate the ratio of the source spread flux to the target central sources,

$$\epsilon_{ij} = S_i \text{PSF}(\delta\alpha \cos(\beta), \delta\beta) / S_j, \quad (6)$$

where  $S_i$  is the flux density of the source around and  $S_j$  is the flux density of the central source,  $(\delta\alpha \cos(\beta), \delta\beta)$  are the separation angle between the two sources in the R.A. and decl. directions. The PSF is assumed to be a Gaussian kernel with  $\sigma_{\text{PSF}} = \theta_{\text{FWHM}} / 2\sqrt{2 \ln 2}$ , where  $\theta_{\text{FWHM}} = 2.9'$  is the Full Width at Half Maximum of FAST prior beam. We set a threshold of  $\epsilon = 0.05$ , i.e. the sources are removed if there is more than one nearby source's point-spread flux density over 5% of target source flux density.

Using the straightforward isolation method, we selected a total of 7 159 sources, e.g., 1 798 from the FATHOMER field and 5 361 from the CRAFTS field. When applying the flux-weighted isolation method, the number of selected

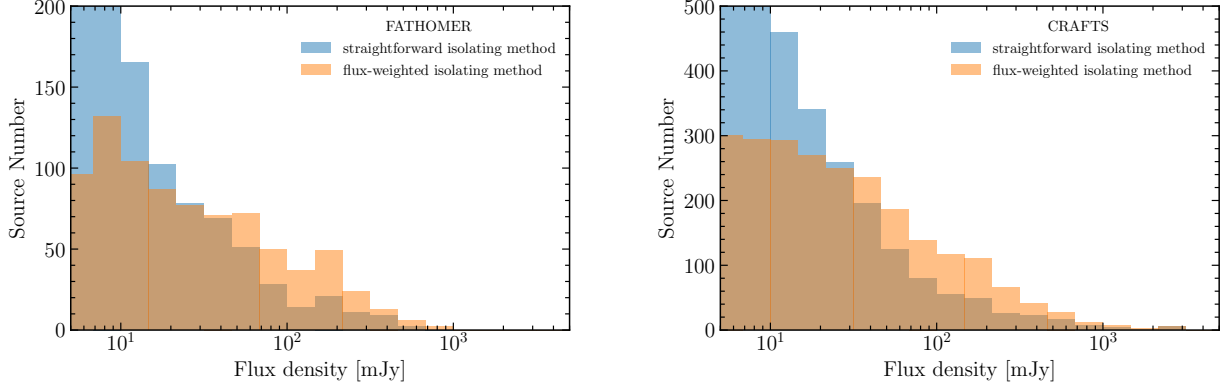


**Figure 1.** The histogram distribution of source number counts for the two source isolating methods. The straightforward isolating method result is shown in blue and the flux-weighted isolating method result is in orange. The left panel shows the results of the FATHOMER dataset and the right panel shows the results of the CRAFTS dataset, respectively.

sources decreased to 4 202, with 1 087 in the FATHOMER field and 3 115 in the CRAFTS field. Figure 1 presents the flux density distribution of sources identified using the two isolation methods. Although the flux-weighted isolation method reduces the total number of sources, it retains more bright sources than the straightforward method, enhancing the quality of beam pattern reconstruction. Applying a final flux limit of 20 mJy, the flux-weighted isolation method selects 1 668 sources, which is 456 more than the straightforward method.

Before proceeding to the beam stacking, we further truncate the time-ordered data and keep a segment of data with only 50 time stamps before and after the transition time, which is defined as the time stamps when the target sources are mostly close to the beam center. It should be noted that each source can be observed multiple times by different beam at different times. Considering the observation duplication, there are  $\sim 960$  and  $\sim 1\,200$  data segments per beam in the FATHOMER and CRAFTS field, respectively, finally used for the beam pattern construction.

### 3.4. Zernike polynomial beam model

We adopt the Zernike polynomial (ZP) modes as the analytic basis and decompose the 2-dimensional beam pattern against these modes. The ZP modes are a sequence of polynomials that are continuous and orthogonal over a unit circle (Zernike 1934). Initially, they were utilized as a mathematical representation of optical wavefronts traversing imaging components (Lakshminarayanan & Fleck 2011), and then employed to characterize the primary beam patterns for radio telescopes (Asad et al. 2021). The ZP modes of order  $n$  and angular frequency  $m$  take the form of,

$$Z_n^m(\rho, \phi) = R_n^m(\rho)e^{im\phi}, \quad (7)$$

where  $(\rho, \phi)$  are the coordinates of the polar frame with origin at the beam center,  $n$  and  $m$  are non-negative integers with

$n > |m|$  and  $n - |m|$  is always even. The radial polynomials  $R_n^{\pm m}(\rho)$  is expressed as,

$$R_n^{\pm m}(\rho) = \sum_{k=0}^{\frac{n-m}{2}} \frac{(-1)^k (n-k)!}{k! (\frac{n+m}{2} - k)! (\frac{n-m}{2} - k)!} \rho^{n-2k}. \quad (8)$$

The beam pattern is constructed as a linear combination of these ZP modes,

$$\hat{\mathbf{B}} = \sum_i^{N_Z} a_i \mathbf{z}_i, \quad (9)$$

where  $\hat{\mathbf{B}}$  is the beam pattern constructed via stacking analysis, i.e. Equation (4),  $i$  denotes the Noll indices (Noll 1976) of the ZP mode  $Z_n^m$ ,  $N_Z$  is the number of ZP modes used for beam model construction,  $\mathbf{z}_i$  denotes the  $i$ -th ZP modes, i.e.  $\mathbf{Z} = \{\mathbf{z}_i\} = \{Z_n^m(\rho, \phi)\}$ , and  $a_i$  represents the corresponding coefficients,

$$\mathbf{A} = \{a_i\} = (\mathbf{Z}^T \mathbf{Z})^{-1} \mathbf{Z} \mathbf{B}. \quad (10)$$

The ZP modes with higher orders represent the extremely small-scale structures, which are noise-dominated. We use the ZP modes up to the 23rd order, which contains three hundred coefficients. In addition, the coefficients of the ZP modes within the first 23 orders vary significantly. In order to improve the signal-to-noise ratio of the beam pattern model, we drop the noise-dominated ZP modes. The detailed noise filtering is presented in Section 4.4.

## 4. RESULTS AND DISCUSSION

The positions of the 19 feeds within the FAST L-band 19-feed array (19FA) frame are shown in Figure 2. Here, the  $H$ -axis and  $V$ -axis correspond to the horizontal and vertical axes. We group the 19 feeds into four subsets according to their separation distance to the feed array center, i.e.

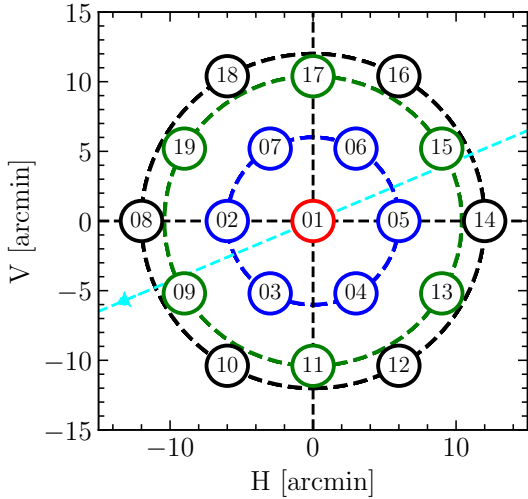


**Figure 2.** The positions of the feeds in the frame of the FAST L-band 19-feed array (19FA). The circles are the FAST beams with the beam size  $2.9'$ . The center, inner-circle, middle-circle, and outer-circle beams are shown in red, blue, green, and black, respectively. The cyan dashed line with an arrow indicates the drift scanning direction along R.A..

as shown in Figure 2, the center beam (red), inner-circle beams (blue), middle-circle beams (green), and the outer-circle beams (black). During the drift scan observation, the feed array rotated by  $23.4^\circ$ . The cyan dashed line with an arrow indicates the drift scanning direction, which is aligned with the R.A. direction in the observational frame.

#### 4.1. The stacking-based beam pattern

To investigate the consistency of the stacking-based beam pattern reconstruction method, we select observations with similar decl. coverage from FATHOMER and CRAFTS. We then perform the stacking analysis separately on each dataset as well as on the combined dataset. We combine the two linear polarizations, i.e. XX and YY, to increase the signal-to-noise ratio. The reconstructed beam patterns are shown in Figure 3, where the results of FATHOMER, CRAFTS, and their combined dataset are shown in the left, middle, and right columns, respectively. From the top to the bottom rows, the results are Beam01, Beam02, Beam19, and Beam08, which are examples of beams located in the center, inner circle, middle circle, and the outer circle of the FAST L-band feed array, respectively. All the beam patterns are shown in the observation frame, where the horizontal and vertical axes are aligned with the R.A. and decl. direction.

The shape of the main beam can be constructed by stacking either with the FATHOMER or CRAFTS dataset. The side lobes of Beam02, Beam19, and Beam08 are also visible with each dataset. However, significant data deficiency, which is due to either lack of observation or RFI flagging, is also visible, especially within the size of the main beam. Such

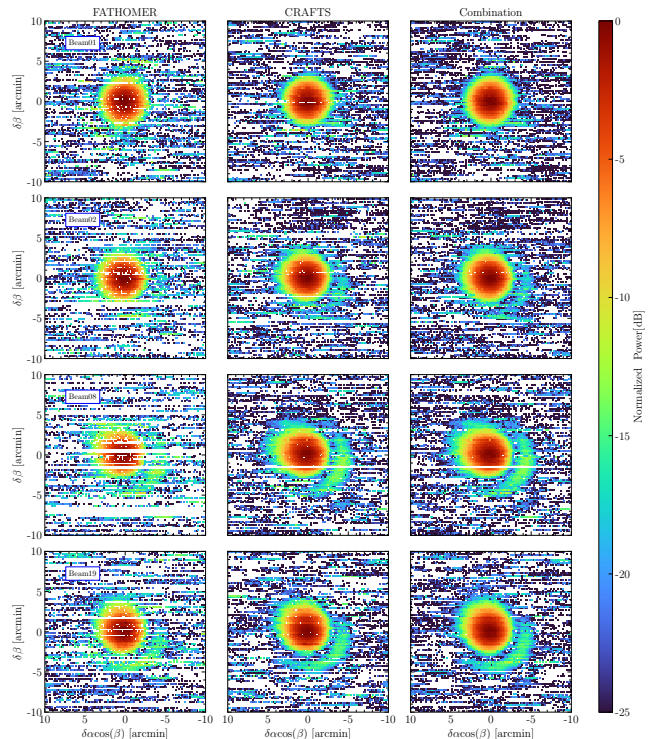


**Figure 3.** The stacked beam patterns for four different beams (Beam01, Beam02, Beam08, and Beam19) obtained from the data between 1375-1425MHz. The four columns represent the data from three different sources: FATHOMER (first column), CRAFTS (second column), and a combination of both (third column). Each row corresponds to a unique beam, with each beam having a distinct distance from the central beam center.

data deficiencies are substantially eliminated by combining the two datasets, as shown in the right columns, where the blank pixels within the main beam are populated with supplementary datasets. The remaining blank pixels outside the main beam are due to the observation noise.

The shapes of the main beam and side lobes show distinct variations across different beam positions. Beam01 displays a symmetric circular main beam profile, while Beam02, Beam08, and Beam19 exhibit more pronounced distortions, each showing an asymmetry with one side compressed and the other elongated. Notably, the side lobe shapes are the most striking feature among the four beams. Beam01's side lobe is suppressed, whereas those of Beam02, Beam08, and Beam19 are visible. The side lobes of Beam08 and Beam19, in particular, are especially pronounced, with clearly discernible contours.

The direction of asymmetry distortion is directly related to the beam's position with respect to the center of the 19FA frame. The greater the distance of the beam from the center of the feed array, the more pronounced the asymmetry of the beam becomes.

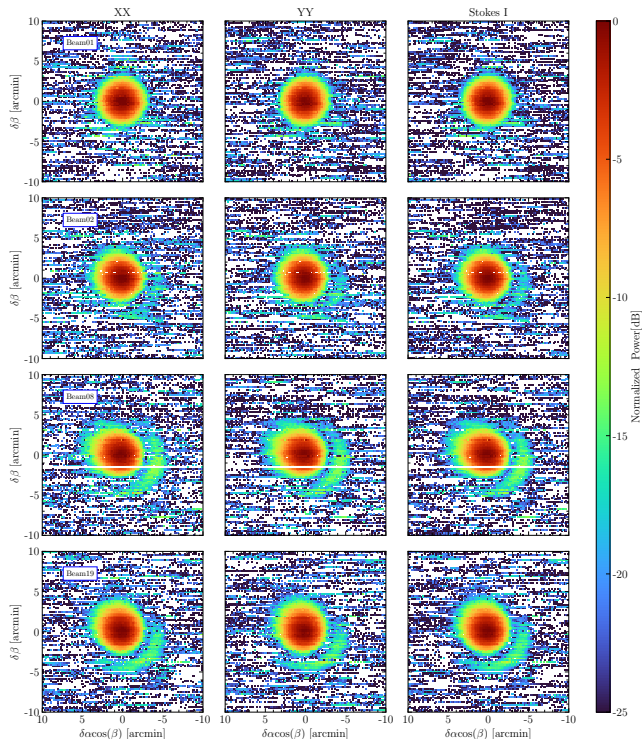


**Figure 4.** The stacked beam patterns for four different beams (Beam01, Beam02, Beam08, and Beam19) obtained from the data between 1375-1425MHz. The four columns represent the polarization results for XX (vertical), YY (horizontal), and Stokes I (total intensity), respectively. Each row corresponds to a unique beam, with each beam having a distinct distance from the central beam center.

In addition to the polarization-combined beam stacking, we also investigate the beam patterns for the XX and YY polarization, individually. As only a few of the selected NVSS sources are significantly polarized, we ignore the polarization fraction and assume equal flux density for each polarization. The results are shown in Figure 4, where the left and middle columns show the beam pattern for XX and YY polarizations. The polarization-combined results are shown as a reference in the right column. Similar to Figure 4, we also inspect the beam patterns of Beam01, Beam02, Beam08, and Beam19, as the examples for the center, inner-circle, outer-circle, and middle-circle beams. All the beam patterns shown in Figure 4 use the combined datasets of FATHOMER and CRAFTS.

We find that the beam features for both XX and YY polarizations are similar, and align with the polarization-combined beam patterns. Given the current sensitivity limit, the differences between polarizations are negligible and we only focus on the polarization-combined beam pattern, i.e. the beam pattern of Stokes I, in the following analysis.

#### 4.2. The beam pattern model

Since the beam pattern shows significant asymmetry, we adopt the ZP modes as the analytical bases to model the beam pattern features. In particular, we use the Python script of `zernike`<sup>7</sup> (Antonello & Verhaegen 2015) to generate the ZP modes and decompose the beam patterns.

As a comparison, we also fit the beam patterns with a circular-symmetric Gaussian profile,

$$B_G(\rho, \phi) = \exp\left(-\frac{1}{2} \frac{\rho^2}{\sigma_G^2}\right), \quad (11)$$

where  $(\rho, \phi)$  are the coordinates of the beam-centered polar frame,  $\sigma_G$  is a free parameter characterizing the beam size and related to the full width at half maximum  $\theta_{\text{FWHM}}$  of the beam pattern via  $\sigma_G = \theta_{\text{FWHM}} / (2\sqrt{2 \ln 2})$ .

To quantify the reconstruction accuracy, we calculate the residual between the measured beam pattern  $\hat{B}(\rho, \phi)$  and the beam model for both the ZP modes and Gaussian profile,

$$r(\rho, \phi) = \hat{B}(\rho, \phi) - B_{\{G,Z\}}(\rho, \phi), \quad (12)$$

where  $\{G, Z\}$  denote the Gaussian and ZP model, respectively. We show examples of the residuals for both the Gaussian model (top panels) and the ZP model (bottom panels) in Figure 5. From the left to the right column, we show the residuals of Beam01, Beam02, Beam19, and Beam08, which are examples of the center beam, inner-circle beams, middle-circle beams, and outer-circle beams, respectively. It is clear that, for the center beam, the Gaussian model and ZP model have similar residual patterns. However, for the beams off the feed array center, there are significant residual patterns for the Gaussian model.

We inspect the residual for all the beams of the same subsets via the statistical histogram distributions with respect to the  $\rho$  bins. In addition, we characterize the residual distribution for the main beam and the first side lobe, separately. According to the FAST beam measurements in the literature, we set a prior of  $\theta_{\text{FWHM}}$ , which corresponds to the radius of the first null, for separating the main beam and side lobes, i.e., for the main beam we use residuals within  $\rho < \theta_{\text{FWHM}}$  and for the side lobe we use  $\theta_{\text{FWHM}} \leq \rho < 2\theta_{\text{FWHM}}$ . The residual statistical histogram as the function of radial distance  $\rho$  for the main beam and first side lobe are shown with the violin plots in the left and right panel of Figure 6, respectively. The residuals for the ZP model are shown in green (left side of the violin plot) and for Gaussian model are shown in blue (right side of the violin plot). In each panel of Figure 6, we show the residual histogram of the beams in the subset of the center beam, inner-circle beams, middle-circle beams, and outer-circle beams, individually.

<sup>7</sup> <https://pypi.org/project/zernike/>

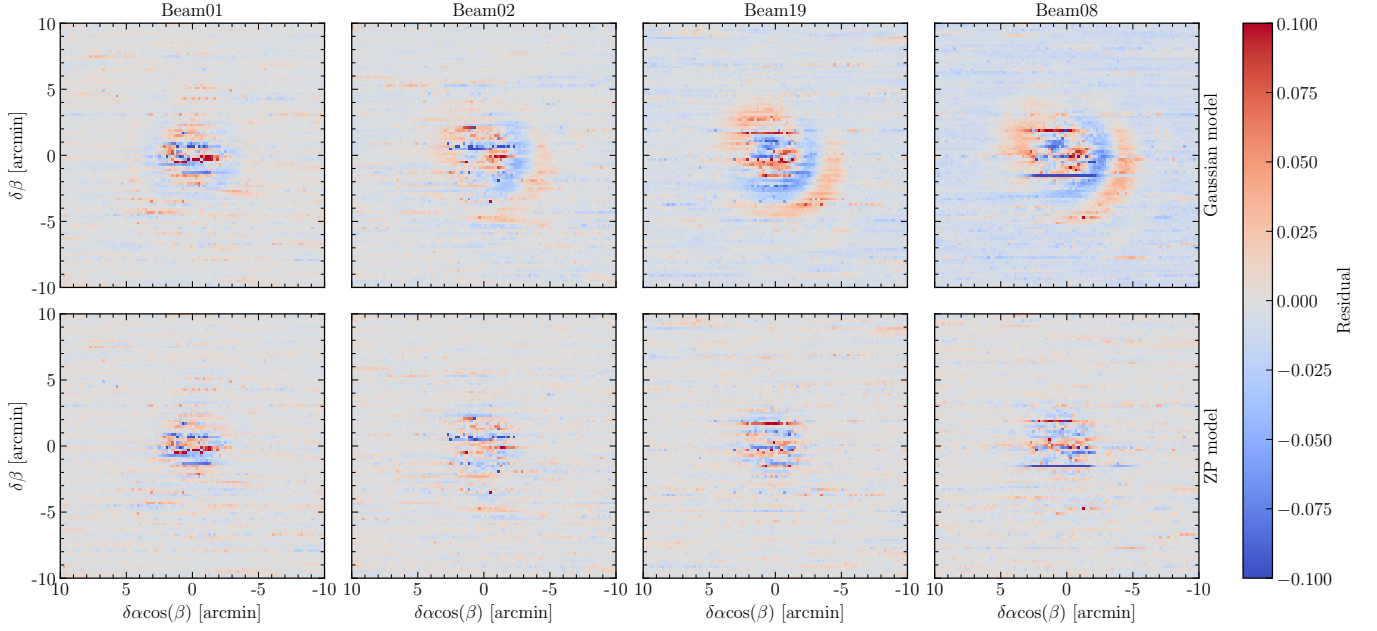


**Figure 5.** The residuals of the measured beam pattern and the fitting models. The top panels show the residuals for the Gaussian model while the bottom panels show the residuals for the ZP model. From the left to the right columns, there are the residuals for Beam01, Beam02, Beam19, and Beam08, which are examples of the subset of the center beam, inner-circle beams, middle-circle beams, and outer-circle beams.

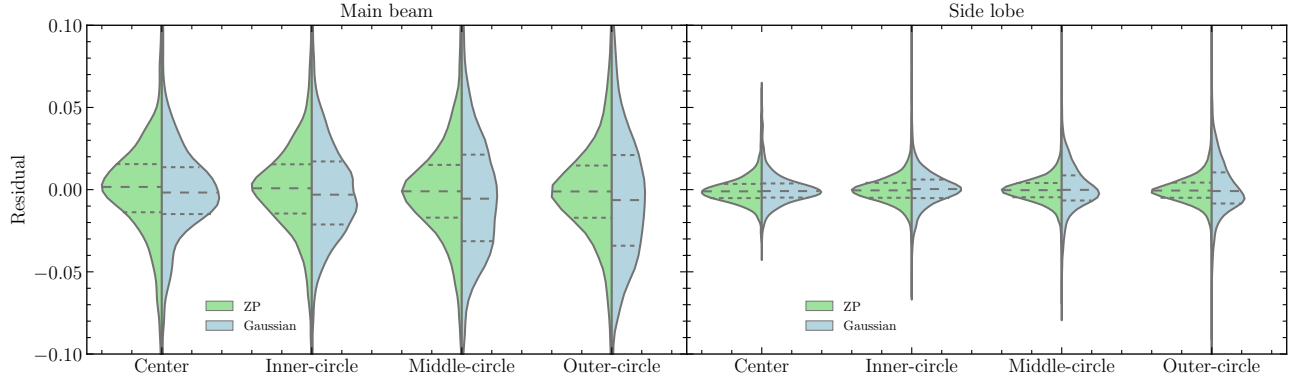


**Figure 6.** The residual histogram distribution of all the beams in the same beam subset, i.e. the center beam, inner-circle beams, middle-circle beams, and outer-circle beams. The residuals for the ZP model are shown in green (left side of the violin plot) and residuals for the Gaussian model are shown in blue (right side of the violin plot). The left panel shows the residuals within the main beam size, i.e.  $\rho < \theta_{\text{FWHM}}$ ; while the right panel shows the residuals of the side lobe, i.e.  $\theta_{\text{FWHM}} \leq \rho < 2\theta_{\text{FWHM}}$ .

Generally, the residuals within the main beam have a broader histogram distribution than that in the side lobe, which is mainly due to the greater absolute values of the main beam.

For the center beam, both models yield similar results, i.e., the residual distributions closely resembled the normal distribution. As long as the beam profile is circularly symmetric and the side lobes are suppressed, the Gaussian profile is still a good approximation of the beam pattern shape.

In contrast, the residual distributions of the off-center beams, e.g., the inner-circle beams, middle-circle beams, and outer-circle beams, reveal significant differences between the

ZP model and the Gaussian model. Particularly, the Gaussian model has residual distributions that deviate from the normal distribution, significantly, which indicates the systematic differences between the Gaussian model and the beam pattern measurements. On the other hand, the ZP model residual behaves in the unique normal distribution for all the beam subsets. The results show that the ZP model successfully characterizes the primary features of the beam pattern for both the symmetric and asymmetric cases.

### 4.3. The ZP mode decomposition



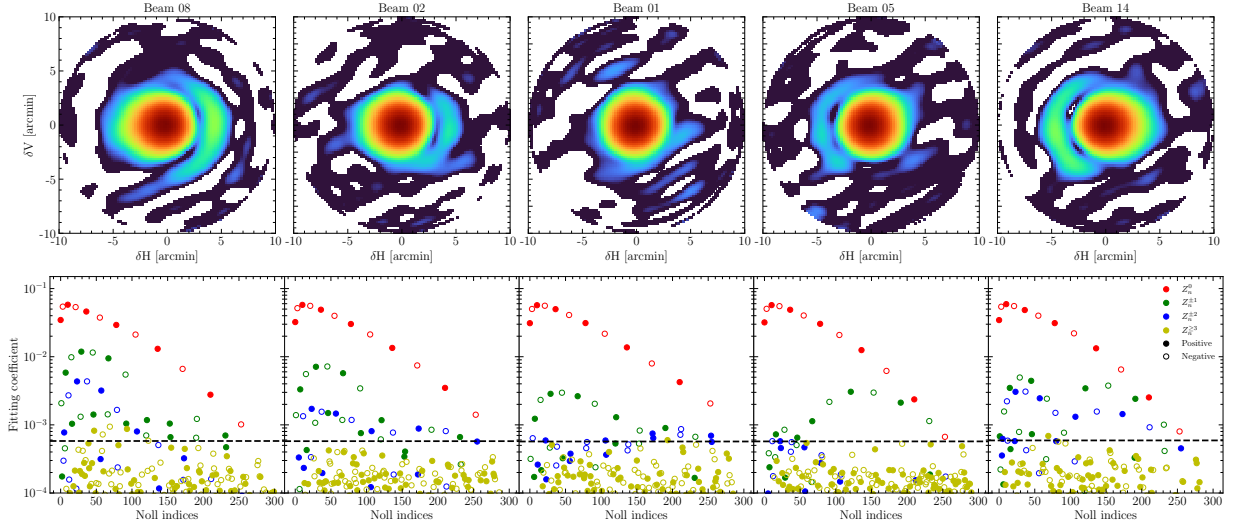


**Figure 7.** Top panels: the constructed beam pattern with the first 23 orders of ZP modes. All the beam patterns are rotated to the 19FA frame. The  $\delta H$ - and  $\delta V$ -axes represent the separation angle in the  $H - V$  axes with respect to the beam center. Bottom panels: the corresponding ZP fitting coefficients shown as the function of Noll indices. The filled markers denote positive coefficients and the empty markers indicate negative coefficients. The colors mark different angular frequencies  $m$ . The horizontal dashed line indicates 1% of the maximum fitting coefficient.

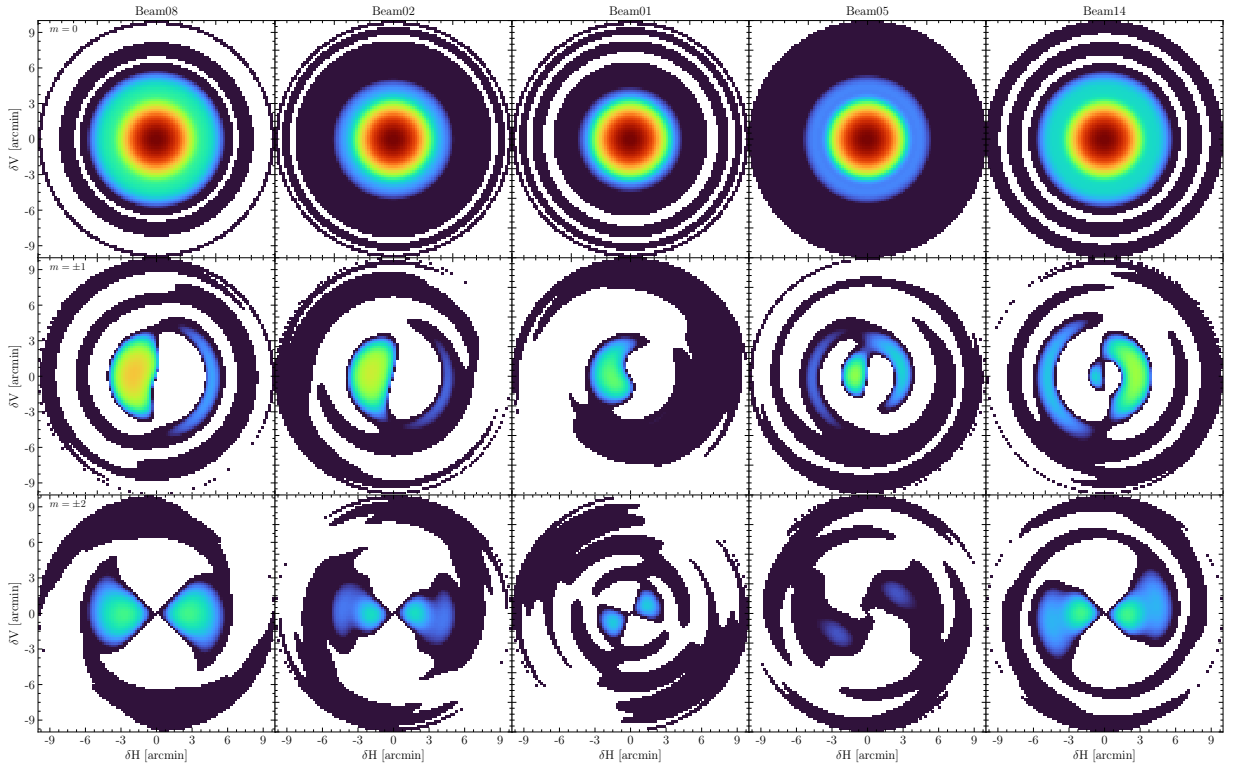


**Figure 8.** The beam pattern constructed with ZP mode of different angular frequency  $m$ , i.e. the beam pattern constructed with ZP modes of  $m = 0$ ,  $m = \pm 1$ , and  $m = \pm 2$  are shown in the top, middle, and bottom rows, respectively.

The top panels of Figure 7 display the ZP-model reconstructed beam patterns, where we display instances of the 5 beams in a row aligned with the  $H$ -axis of the 19FA frame. We rotate the beam pattern from the observation frame to the 19FA frame. The center beam shows a circularly symmetric main beam profile and suppressed side lobes, while the off-center beams show significant asymmetry and pronounced side lobes. The side lobes of the off-center beams are distinctly pronounced toward the center of the 19FA frame, and the beam distortion aligns with the radial direction of the frame.

The bottom panels display the fitting coefficients with respect to the Noll indices, up to 300, which is corresponding to the first 23 orders of the ZP modes. The ZP modes with lower Noll indices correspond to the smaller variation structures. By analyzing the coefficients of these polynomials, we can gain insights into the beam pattern structures and their relationship to the side lobe intensities. Specifically, the variation in the coefficients of the polynomials with circular frequency  $m$  across different beams suggests that the beam pattern structure is not uniform and is influenced by various factors.

The fitting coefficients of the ZP modes with angular frequencies  $m = 0, \pm 1, \pm 2$ , and  $|m| \geq 3$  are plotted in red, green, blue, and yellow, respectively. The solid and empty markers distinguish the positive and negative values, respectively. As shown in the plot, the ZP modes with an angular frequency  $m = 0$  exhibit relatively large coefficients for all the beams, which demonstrates the beam patterns are primarily characterized by such ZP modes. We display the beam patterns constructed with only the ZP modes of  $m = 0$  in the top rows of Figure 8. The ZP modes of  $m = 0$  characterize the circularly symmetric features of the beam patterns.

The circular asymmetric features are characterized by the ZP modes with  $m \neq 0$ . As shown in Figure 7, the corresponding fitting coefficients of such modes, i.e.,  $Z_n^{\pm 1}$ ,  $Z_n^{\pm 2}$ , and  $Z_n^{|m| \geq 3}$ , are significantly lower than the coefficients of  $Z_n^0$ . Moreover, the center beam exhibits even lower fitting coefficients for the ZP modes with  $m \neq 0$  than the off-center beams. The beam patterns constructed with only the ZP modes of  $m = \pm 1$  and  $m = \pm 2$  are shown in the middle and bottom rows of Figure 8. The asymmetric features primarily characterize the distortion of the main beam and the side lobes. Notably, as shown in the middle panels of such two rows, there are weak asymmetry features in the center beams, which indicates a slight distortion of the center beam. The origin of such center beam distortion is worth further investigating in the future with more observation data.

#### 4.4. The noise-filtered beam pattern

The fitting coefficients of ZP modes with  $|m| \geq 3$ , as shown with the yellow markers in Figure 7, are mostly lower than

1% of the maximum fitting coefficients. ZP modes with  $|m| \geq 3$  generally characterize highly oscillated structures. Although such structures are tiny compared to the main beam profile, it is still important to be fully characterized for future H<sub>I</sub> IM experiments. However, given current measurement uncertainties, such weak structures are mostly dominated by observational noise. The equipment's thermal noise is one of the origins of measurement uncertainty. On the other hand, the flux density variation of the NVSS sources potentially impacts the measurement. Both the thermal noise and flux density variation are systematic and can be eliminated via a large amount of observation. In this work, we drop the ZP modes with fitting coefficients less than 1% of the maximum fitting coefficients. Eventually, the number of ZP modes adopted varies across different beams. The central beam has 31 ZP modes, which is the minimal number of ZP modes. The ZP mode numbers increase with the beam getting further from the feed array center, e.g., the inner-circle beams have  $\sim 33$  ZP modes on average, and the middle- and outer-circle beams have  $\sim 44$  on average, respectively. The noise-filtered beam patterns for all the 19 feeds are shown in Figure 9, where the relative positions of the panels correspond to the feed pointing direction in the sky. All the beam patterns are rotated to the feed coordinates. The yellow, green, and blue contours in each panel indicate the 50%, 10%, and 1% of the maximum, respectively. As discussed in Section 4.1, we focus on the Stokes I component and all the beam patterns are averaged across the frequency range of 1375 MHz – 1425 MHz.

The yellow contours in each panel indicate the beam pattern at 50% of their maximum, which is commonly defined as the beam size of full width at half maximum. The beam profiles within the 50% contour show unique circular symmetric and the differences between the 19 beams are negligible.

The beam patterns between the 10% and the 1% contours are identified as the side lobes. Significantly, the side lobe profiles vary across the 19 beams. After filtering out the noise components, the asymmetric side lobe profiles are clearer than those shown in Section 4.1. The side lobes are getting more pronounced with the larger separation distance between the beam and the feed array center. In addition, the direction of the side lobe distortion relates to the feed array's relative position. Specifically, the side lobes become more pronounced on the side of the beam closer to the center of the feed array along the radial direction. Although the circular symmetry of the off-center beam is disrupted, the beam pattern still retains axial symmetry, with its axis of symmetry aligned with the radial direction of the feed array.

The ZP mode coefficients of the noise-filtered beam model can be accessed from the GitHub repository Fast19FABM <sup>8</sup>.

<sup>8</sup> <https://github.com/Nyarlth/Fast19FABM>.

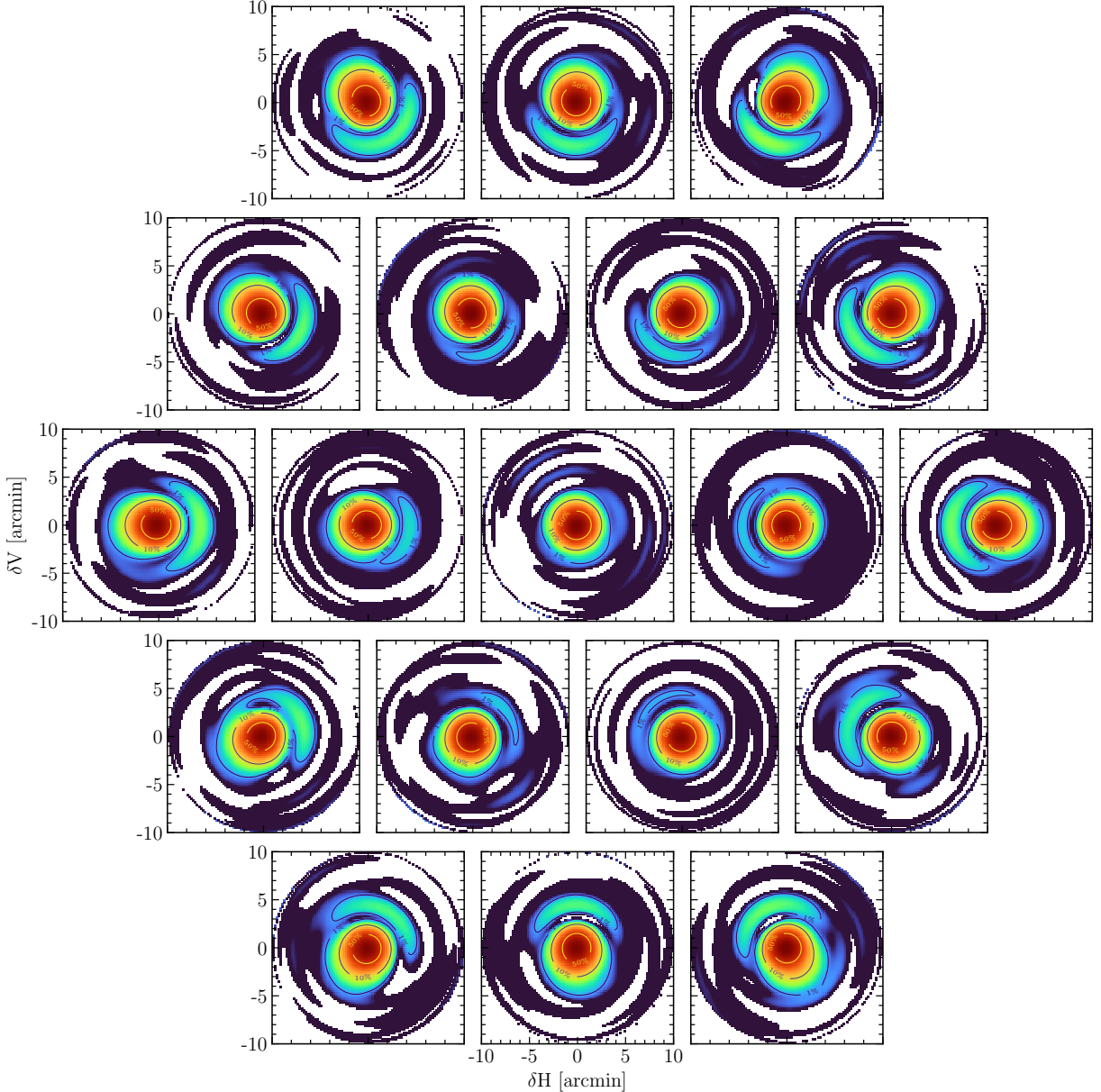


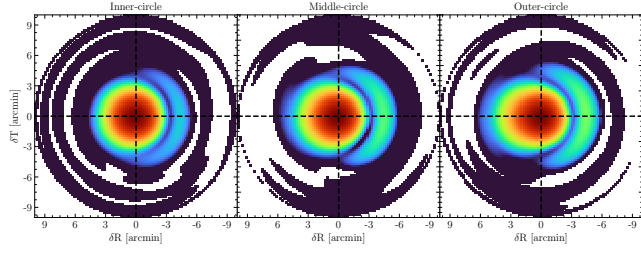
**Figure 9.** The noise-filtered beam pattern of all the 19 beams of the FAST L-band feed array. The beam patterns are rotated to align with the 19FA frame. The positions of the beams correspond to their projected pointing direction in the sky. The yellow, green, and blue contours represent the 50%, 10%, and 1% of maximum response value at the beam center.

#### 4.5. The side lobes

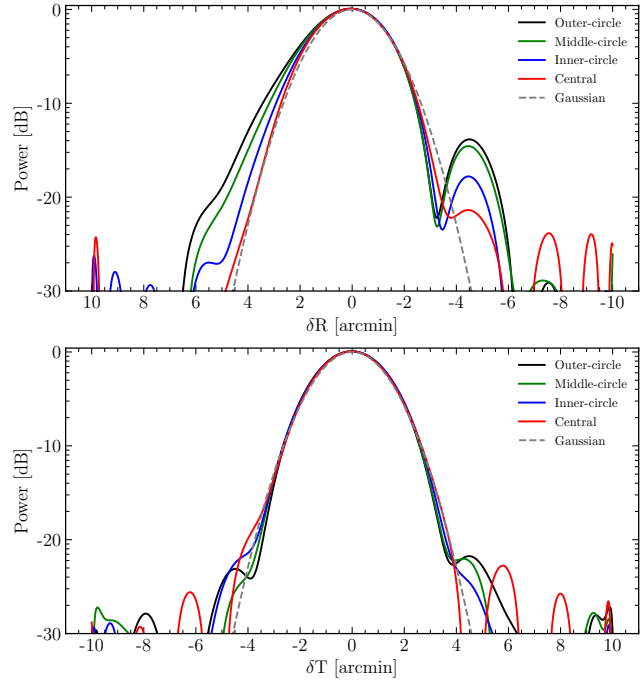
In this work, we group the 19 feeds into four beam subsets, i.e., as shown in Figure 2, the center beam, inner-circle beams, middle-circle beams, and outer-circle beams. To emphasize the major features of each beam subset, we stack the beam patterns of the same subset. Because the beam pattern still retains axial symmetry, with its axis of symmetry aligned with the radial direction of the feed array, we rotate and stack the off-center beams in the  $R-T$  coordinates, where  $R$  and  $T$  represent the radial and tangential directions of the 19FA frame. The subset-stacked beam patterns are shown in

Figure 10, where  $\delta R$  and  $\delta T$  represent the separation angle with respect to the beam center along the  $R$  and  $T$  axes. We further extract the beam profile along the horizontal and vertical dashed lines as the radial and tangential direction beam profiles. The radial and tangential direction beam profiles for each beam subset are shown in the top and bottom panels of Figure 11, respectively.

In Figure 11, as a reference, we plot a Gaussian profile with  $\theta_{\text{FWHM}} = 2.9'$  in dashed gray line. The radial and tangential central beam profiles are the same and are constructed by circular averaging of the center beam pattern. There is



**Figure 10.** The beam pattern stacked with the beam in the subset of inner-circle (left panel), middle-circle (middle panel), and outer-circle (right panel) beams. The horizontal and vertical black dashed lines indicate the radial and tangential direction of the 19FA frame, respectively.



**Figure 11.** The stacked beam profiles along the radial (top panel) and tangential (bottom panel) directions of the 19FA frame.  $\delta R$  and  $\delta T$  axes indicate the separation angle with respect to the beam center along the radial and tangential directions, respectively. The beam profiles for different beam subsets are shown in different colors. The central beam profile is constructed by circular averaging of the center beam pattern and it is the same for the radial and tangential profile. The Gaussian profile is assumed to have  $\theta_{\text{FWHM}}$  is  $2.9'$ , the prior angular resolution of FAST at 1400 MHz.

a significant deviation from the symmetric Gaussian beam profile for the off-center beams in the radial direction, while the tangential direction shows minor deviations.

For the radial beam profile, the center beam shows several side lobes and its first side lobe is weak and connected with the main beam profile. The off-center beams display a prominent first side lobe on the side close to the center of the feed array. On average, the inner-circle, middle-circle,

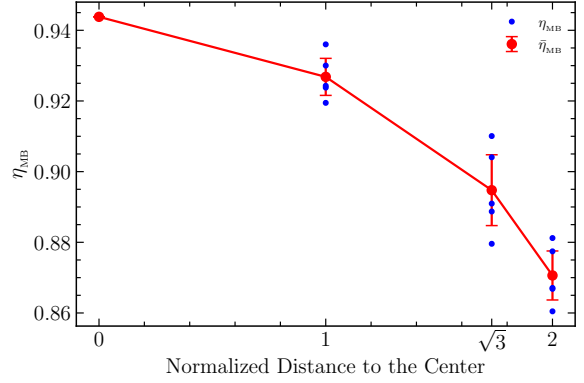


**Figure 12.** The main beam efficiency of 19 beams. The  $x$ -axis represents the distance to the feed array center normalized with the radius of the inner circle. The main beam efficiency of the center beam, inner-circle beams, middle-circle beams, and the outer-circle beams are shown with  $x = 0, 1, \sqrt{3},$  and  $2$ , respectively. The red error bars indicate the mean and standard deviation of the main beam efficiency across the beams in the same subset.

and outer-circle beams exhibit the first side lobes peaked at  $\delta R = -4.455'$ ,  $\delta R = -4.455'$ , and  $\delta R = -4.495'$ , with amplitudes of  $-17.79\text{dB}$ ,  $-14.56\text{dB}$ , and  $-13.84\text{dB}$  with respect to the beam center, respectively. In addition, the middle-circle and outer-circle beams also show the second side lobes at  $\delta R = -7.317'$  and  $\delta R = -7.538'$ , with amplitudes of  $-28.88\text{ dB}$  and  $-29.11\text{ dB}$ , respectively.

#### 4.6. Main beam efficiency

The beam pattern distortion and the prominent side lobes affect the main beam efficiency. We estimate the main beam efficiency  $\eta_{\text{MB}} = \Omega_{\text{MB}}/\Omega_{\text{A}}$ , where  $\Omega_{\text{MB}}$  is the main beam solid angle and  $\Omega_{\text{A}}$  is the full beam solid angle. According to the noise-filtered beam patterns in Figure 9, the beam patterns decline to below 0.5% of the maximum beam pattern with  $\rho \geq 6'$ . We estimate the full beam solid angle by integrating the beam profile with  $\rho < 10'$ . In addition, we define the main beam size according to the center beam, i.e., the circular region with  $\rho \leq \theta_{\text{FWHM}}$ , is defined as the main beam, which is close to the size of the first null.

The main beam efficiencies of the 19 beams are shown with the blue markers in Figure 12. The  $x$ -axis represents the distance to the feed array center normalized with the radius of the inner circle, and the beams in each subset, i.e., the center beam, inner-circle beams, middle-circle beams, and the outer-circle beams, are shown with  $x = 0, 1, \sqrt{3},$  and  $2$ . The red error bars indicate the mean and the standard deviation of the main beam efficiencies of the same beam subset. The central beam has the main beam efficiency  $\eta = 0.944$ . The mean main beam efficiency decreases to 0.927, 0.895, and 0.871 for the beams in inner-circle, middle-circle, and outer-circle beam subsets, respectively. The decreases in the main beam

efficiency for the off-center beams are primarily due to the growing side lobes. However, it is corresponding to 1.7%, 4.9%, and 7.3% decreases with respect to the center beam's efficiency, which is a minor declination.

The main beam efficiency of FAST L-band 19 feeds measured in the literature varies, e.g. at the range 65% to 85% from Gao et al. (2022) or at the range from 80% to 95% Sun et al. (2021). The variation is likely caused by the measurement uncertainties of the noise diode. The value increases overall as the observation frequency increases and the main beam efficiency decreases as the beam moves away from the center, with the central beam having the maximum efficiency (Gao et al. 2022). In this research, we consider the unique beam patterns of the FAST L-band 19 feeds and use numerical integration to calculate the main beam efficiency  $\eta_{\text{MB}}$ . Our results are comparable with the measurement in the literature, in particular, consistent with Sun et al. (2021).

## 5. CONCLUSION

This is the second in a series of papers focusing on intensity mapping in the FAST using drift scan surveys. In this paper, we utilize the drift scan observation data from the FATHOMER (Li et al. 2023), as well as the data from CRAFTS (Li et al. 2018), preprocessed with the pipeline developed in our previous work (Li et al. 2023), to reconstruct the beam model for the FAST 19FA.

We develop a beam reconstruction method based on stacking analysis. This approach utilizes drift-scan observational data, adopting radio continuum point sources within the drift-scan field, such as NVSS sources, to reconstruct the antenna's beam pattern. This method minimizes the impact of beam variations caused by changes in antenna configuration on actual observations, thus optimizing the accuracy of beam measurement.

We adopt the ZP modes as the analytic basis and decompose the two-dimensional beam pattern using these modes. ZP modes with fitting coefficients below 1% of the maximum coefficient are discarded. Specifically, 31 ZP modes are used to construct the central beam pattern; on average, approximately 33 ZP modes are used for the inner-circle beams, and around 44 ZP modes for the middle- and outer-circle beams.

The center beam exhibits a circularly symmetric beam profile with suppressed side lobes, which can be well modeled with a Gaussian beam profile. For the off-center beams, the

side lobes are getting more pronounced with the larger separation distance between the beam and the feed array center. In addition, the side lobes become more pronounced on the side of the beam closer to the center of the feed array along the radial direction. Although the circular symmetry of the off-center beam is disrupted, the beam pattern still retains axial symmetry, with its axis of symmetry aligned with the radial direction of the feed array.

We found the first side lobes averaged across the same beam subsets, i.e. the inner-circle, middle-circle, and outer-circle beam subsets, peaked at  $\delta R = -4.455'$ ,  $\delta R = -4.455'$ , and  $\delta R = -4.495'$ , with amplitudes of  $-17.79\text{dB}$ ,  $-14.56\text{dB}$ , and  $-13.84\text{dB}$  with respect to the beam center, respectively. The corresponding main beam efficiencies slightly decrease by 1.7%, 4.9%, and 7.3% with respect to the center beam's efficiency.

Given the current sensitivity limits, we focus exclusively on the Stokes I beam pattern, averaged over the frequency range of 1375—1425 MHz. With additional drift-scan observational data, our stacking-based beam reconstruction method could also facilitate studies of polarized beam patterns and their frequency dependence.

## ACKNOWLEDGEMENTS

This work made use of the data from FAST (Five-hundred-meter Aperture Spherical radio Telescope). FAST is a Chinese national mega-science facility, operated by National Astronomical Observatories, Chinese Academy of Sciences. We acknowledge the support of the National SKA Program of China (Nos. 2022SKA0110200, 2022SKA0110202, 2022SKA0110203, 2022SKA0110100, 2022SKA0110101), the NSFC International (Regional) Cooperation and Exchange Project (No. 12361141814), the 111 Project (No. B16009), and the National Natural Science Foundation of China (Nos. 12473091, 11975072, 11835009, 12473001). X. Sun acknowledges the support of the NSFC (grand No. 12433006).

## DATA AVAILABILITY

The FAST 19FA beam models presented in this paper can be accessed from repository Fast19FABM: <https://github.com/Nyarlth/Fast19FABM>. The data underlying this article will be shared on reasonable request to the corresponding author.

## REFERENCES

- Amiri, M., Bandura, K., Boskovic, A., et al. 2022, The Astrophysical Journal, 932, 100, doi: [10.3847/1538-4357/ac6b9f](https://doi.org/10.3847/1538-4357/ac6b9f)
- Amiri, M., Bandura, K., Chen, T., et al. 2023, The Astrophysical Journal, 947, 16, doi: [10.3847/1538-4357/acb13f](https://doi.org/10.3847/1538-4357/acb13f)
- Amiri, M., Chakraborty, A., Foreman, S., et al. 2024, arXiv e-prints, arXiv:2408.00172, doi: [10.48550/arXiv.2408.00172](https://doi.org/10.48550/arXiv.2408.00172)
- Anderson, C. J., Luciw, N. J., Li, Y. C., et al. 2018, Monthly Notices of the Royal Astronomical Society, 476, 3382, doi: [10.1093/mnras/sty346](https://doi.org/10.1093/mnras/sty346)

- Ansari, R., Campagne, J. E., Colom, P., et al. 2012, *Astronomy and Astrophysics*, 540, A129, doi: [10.1051/0004-6361/201117837](https://doi.org/10.1051/0004-6361/201117837)
- Antonello, J., & Verhaegen, M. 2015, *Journal of the Optical Society of America A*, 32, 1160, doi: [10.1364/JOSAA.32.001160](https://doi.org/10.1364/JOSAA.32.001160)
- Asad, K. M. B., Girard, J. N., de Villiers, M., et al. 2021, *Monthly Notices of the Royal Astronomical Society*, 502, 2970, doi: [10.1093/mnras/stab104](https://doi.org/10.1093/mnras/stab104)
- Bagla, J. S., Khandai, N., & Datta, K. K. 2010, *Monthly Notices of the Royal Astronomical Society*, 407, 567, doi: [10.1111/j.1365-2966.2010.16933.x](https://doi.org/10.1111/j.1365-2966.2010.16933.x)
- Bandura, K., Addison, G. E., Amiri, M., et al. 2014, in *Society of Photo-Optical Instrumentation Engineers (SPIE) Conference Series*, Vol. 9145, *Ground-based and Airborne Telescopes V*, ed. L. M. Stepp, R. Gilmozzi, & H. J. Hall, 914522, doi: [10.1117/12.2054950](https://doi.org/10.1117/12.2054950)
- Battye, R. A., Browne, I. W. A., Dickinson, C., et al. 2013, *Monthly Notices of the Royal Astronomical Society*, 434, 1239, doi: [10.1093/mnras/stt1082](https://doi.org/10.1093/mnras/stt1082)
- Battye, R. A., Davies, R. D., & Weller, J. 2004, *Monthly Notices of the Royal Astronomical Society*, 355, 1339, doi: [10.1111/j.1365-2966.2004.08416.x](https://doi.org/10.1111/j.1365-2966.2004.08416.x)
- Bowman, J. D., Morales, M. F., & Hewitt, J. N. 2009, *The Astrophysical Journal*, 695, 183, doi: [10.1088/0004-637X/695/1/183](https://doi.org/10.1088/0004-637X/695/1/183)
- Bull, P., Ferreira, P. G., Patel, P., & Santos, M. G. 2015, *The Astrophysical Journal*, 803, 21, doi: [10.1088/0004-637X/803/1/21](https://doi.org/10.1088/0004-637X/803/1/21)
- Chang, T.-C., Pen, U.-L., Bandura, K., & Peterson, J. B. 2010, *Nature*, 466, 463, doi: [10.1038/nature09187](https://doi.org/10.1038/nature09187)
- Chang, T.-C., Pen, U.-L., Peterson, J. B., & McDonald, P. 2008, *Physical Review Letter*, 100, 091303, doi: [10.1103/PhysRevLett.100.091303](https://doi.org/10.1103/PhysRevLett.100.091303)
- Chen, X. 2012, in *International Journal of Modern Physics Conference Series*, Vol. 12, *International Journal of Modern Physics Conference Series*, 256–263, doi: [10.1142/S2010194512006459](https://doi.org/10.1142/S2010194512006459)
- Chen, Z., Chapman, E., Wolz, L., & Mazumder, A. 2023, *Monthly Notices of the Royal Astronomical Society*, 524, 3724, doi: [10.1093/mnras/stad2102](https://doi.org/10.1093/mnras/stad2102)
- Condon, J. J., Cotton, W. D., Greisen, E. W., et al. 1998, *The NRAO VLA Sky Survey*, doi: [10.1086/300337](https://doi.org/10.1086/300337)
- Cunnington, S., Irfan, M. O., Carucci, I. P., Pourtsidou, A., & Bobin, J. 2021, *Monthly Notices of the Royal Astronomical Society*, 504, 208, doi: [10.1093/mnras/stab856](https://doi.org/10.1093/mnras/stab856)
- Cunnington, S., Li, Y., Santos, M. G., et al. 2023, *Monthly Notices of the Royal Astronomical Society*, 518, 6262, doi: [10.1093/mnras/stac3060](https://doi.org/10.1093/mnras/stac3060)
- Dong, B., & Han, J. L. 2013, *Publications Astronomical Society of Australia*, 30, e041, doi: [10.1017/pasa.2013.19](https://doi.org/10.1017/pasa.2013.19)
- Gao, L.-Y., Li, Y., Ni, S., & Zhang, X. 2023, *Monthly Notices of the Royal Astronomical Society*, 525, 5278, doi: [10.1093/mnras/stad2646](https://doi.org/10.1093/mnras/stad2646)
- Gao, X., Reich, W., Sun, X., et al. 2022, *Science China Physics, Mechanics, and Astronomy*, 65, 129705, doi: [10.1007/s11433-022-2031-7](https://doi.org/10.1007/s11433-022-2031-7)
- Hu, W., Wang, X., Wu, F., et al. 2020, *Monthly Notices of the Royal Astronomical Society*, 493, 5854, doi: [10.1093/mnras/staa650](https://doi.org/10.1093/mnras/staa650)
- Iheanetu, K., Girard, J. N., Smirnov, O., et al. 2019, *Monthly Notices of the Royal Astronomical Society*, 485, 4107, doi: [10.1093/mnras/stz702](https://doi.org/10.1093/mnras/stz702)
- Irfan, M. O., Li, Y., Santos, M. G., et al. 2024, *Monthly Notices of the Royal Astronomical Society*, 527, 4717, doi: [10.1093/mnras/stad3457](https://doi.org/10.1093/mnras/stad3457)
- Jiang, P., Tang, N.-Y., Hou, L.-G., et al. 2020, *Research in Astronomy and Astrophysics*, 20, 064, doi: [10.1088/1674-4527/20/5/64](https://doi.org/10.1088/1674-4527/20/5/64)
- Jin, S.-J., He, D.-Z., Xu, Y., Zhang, J.-F., & Zhang, X. 2020, *Journal of Cosmology and Astroparticle Physics*, 2020, 051, doi: [10.1088/1475-7516/2020/03/051](https://doi.org/10.1088/1475-7516/2020/03/051)
- Jin, S.-J., Wang, L.-F., Wu, P.-J., Zhang, J.-F., & Zhang, X. 2021, *Phys. Rev. D*, 104, 103507, doi: [10.1103/PhysRevD.104.103507](https://doi.org/10.1103/PhysRevD.104.103507)
- Kimball, A. E., & Ivezić, Ž. 2008, *The Astronomical Journal*, 136, 684, doi: [10.1088/0004-6256/136/2/684](https://doi.org/10.1088/0004-6256/136/2/684)
- Lakshminarayanan, V., & Fleck, A. 2011, *Journal of Modern Optics*, 58, 545, doi: [10.1080/09500340.2011.554896](https://doi.org/10.1080/09500340.2011.554896)
- Li, D., & Pan, Z. 2016, *Radio Science*, 51, 1060, doi: [10.1002/2015RS005877](https://doi.org/10.1002/2015RS005877)
- Li, D., Wang, P., Qian, L., et al. 2018, *IEEE Microwave Magazine*, 19, 112, doi: [10.1109/MMM.2018.2802178](https://doi.org/10.1109/MMM.2018.2802178)
- Li, J., Zuo, S., Wu, F., et al. 2020, *Science China Physics, Mechanics, and Astronomy*, 63, 129862, doi: [10.1007/s11433-020-1594-8](https://doi.org/10.1007/s11433-020-1594-8)
- Li, Y., Santos, M. G., Grainge, K., Harper, S., & Wang, J. 2021, *Monthly Notices of the Royal Astronomical Society*, 501, 4344, doi: [10.1093/mnras/staa3856](https://doi.org/10.1093/mnras/staa3856)
- Li, Y., Wang, Y., Deng, F., et al. 2023, *The Astrophysical Journal*, 954, 139, doi: [10.3847/1538-4357/ace896](https://doi.org/10.3847/1538-4357/ace896)
- Li, Y.-C., & Ma, Y.-Z. 2017, *Physical Review D*, 96, 063525, doi: [10.1103/PhysRevD.96.063525](https://doi.org/10.1103/PhysRevD.96.063525)
- Lidz, A., Furlanetto, S. R., Oh, S. P., et al. 2011, *The Astrophysical Journal*, 741, 70, doi: [10.1088/0004-637X/741/2/70](https://doi.org/10.1088/0004-637X/741/2/70)
- Loeb, A., & Wyithe, J. S. B. 2008, *Physical Review Letter*, 100, 161301, doi: [10.1103/PhysRevLett.100.161301](https://doi.org/10.1103/PhysRevLett.100.161301)
- Mao, Y., Tegmark, M., McQuinn, M., Zaldarriaga, M., & Zahn, O. 2008, *Physical Review D*, 78, 023529, doi: [10.1103/PhysRevD.78.023529](https://doi.org/10.1103/PhysRevD.78.023529)
- Masui, K. W., Switzer, E. R., Banavar, N., et al. 2013, *Astrophysical Journal Letters*, 763, L20, doi: [10.1088/2041-8205/763/1/L20](https://doi.org/10.1088/2041-8205/763/1/L20)

- Matshawule, S. D., Spinelli, M., Santos, M. G., & Ngobese, S. 2021, *Monthly Notices of the Royal Astronomical Society*, 506, 5075, doi: [10.1093/mnras/stab1688](https://doi.org/10.1093/mnras/stab1688)
- McQuinn, M., Zahn, O., Zaldarriaga, M., Hernquist, L., & Furlanetto, S. R. 2006, *The Astrophysical Journal*, 653, 815, doi: [10.1086/505167](https://doi.org/10.1086/505167)
- Nan, R., Li, D., Jin, C., et al. 2011, *International Journal of Modern Physics D*, 20, 989, doi: [10.1142/S0218271811019335](https://doi.org/10.1142/S0218271811019335)
- Newburgh, L. B., Bandura, K., Bucher, M. A., et al. 2016, in *Society of Photo-Optical Instrumentation Engineers (SPIE) Conference Series*, Vol. 9906, *Ground-based and Airborne Telescopes VI*, ed. H. J. Hall, R. Gilmozzi, & H. K. Marshall, 99065X, doi: [10.1117/12.2234286](https://doi.org/10.1117/12.2234286)
- Ni, S., Li, Y., Gao, L.-Y., & Zhang, X. 2022, *The Astrophysical Journal*, 934, 83, doi: [10.3847/1538-4357/ac7a34](https://doi.org/10.3847/1538-4357/ac7a34)
- Noll, R. J. 1976, *Journal of the Optical Society of America* (1917-1983), 66, 207
- Pan, J.-D., Wu, P.-J., Du, G.-H., Li, Y., & Zhang, X. 2024, arXiv e-prints, arXiv:2408.00268, doi: [10.48550/arXiv.2408.00268](https://doi.org/10.48550/arXiv.2408.00268)
- Paul, S., Santos, M. G., Chen, Z., & Wolz, L. 2023, arXiv e-prints, arXiv:2301.11943, doi: [10.48550/arXiv.2301.11943](https://doi.org/10.48550/arXiv.2301.11943)
- Paul, S., Santos, M. G., Townsend, J., et al. 2021, *Monthly Notices of the Royal Astronomical Society*, 505, 2039, doi: [10.1093/mnras/stab1089](https://doi.org/10.1093/mnras/stab1089)
- Perdereau, O., Ansari, R., Stebbins, A., et al. 2022, *Monthly Notices of the Royal Astronomical Society*, 517, 4637, doi: [10.1093/mnras/stac2832](https://doi.org/10.1093/mnras/stac2832)
- Peterson, J. B., Aleksan, R., Ansari, R., et al. 2009, in *astro2010: The Astronomy and Astrophysics Decadal Survey*, Vol. 2010, 234. <https://arxiv.org/abs/0902.3091>
- Pritchard, J. R., & Loeb, A. 2008, *Physical Review D*, 78, 103511, doi: [10.1103/PhysRevD.78.103511](https://doi.org/10.1103/PhysRevD.78.103511)
- . 2012, *Reports on Progress in Physics*, 75, 086901, doi: [10.1088/0034-4885/75/8/086901](https://doi.org/10.1088/0034-4885/75/8/086901)
- Reid, B., Ho, S., Padmanabhan, N., et al. 2016, *Monthly Notices of the Royal Astronomical Society*, 455, 1553, doi: [10.1093/mnras/stv2382](https://doi.org/10.1093/mnras/stv2382)
- Santos, M., Bull, P., Alonso, D., et al. 2015, in *Advancing Astrophysics with the Square Kilometre Array (AASKA14)*, 19. <https://arxiv.org/abs/1501.03989>
- Seo, H.-J., Dodelson, S., Marriner, J., et al. 2010, *The Astrophysical Journal*, 721, 164, doi: [10.1088/0004-637X/721/1/164](https://doi.org/10.1088/0004-637X/721/1/164)
- Spinelli, M., Carucci, I. P., Cunnington, S., et al. 2022, *Monthly Notices of the Royal Astronomical Society*, 509, 2048, doi: [10.1093/mnras/stab3064](https://doi.org/10.1093/mnras/stab3064)
- Square Kilometre Array Cosmology Science Working Group, Bacon, D. J., Battye, R. A., et al. 2020, *Publications Astronomical Society of Australia*, 37, e007, doi: [10.1017/pasa.2019.51](https://doi.org/10.1017/pasa.2019.51)
- Sun, S., Li, J., Wu, F., et al. 2022, *Research in Astronomy and Astrophysics*, 22, 065020, doi: [10.1088/1674-4527/ac684d](https://doi.org/10.1088/1674-4527/ac684d)
- Sun, X.-H., Meng, M.-N., Gao, X.-Y., et al. 2021, *Research in Astronomy and Astrophysics*, 21, 282, doi: [10.1088/1674-4527/21/11/282](https://doi.org/10.1088/1674-4527/21/11/282)
- Switzer, E. R., Masui, K. W., Bandura, K., et al. 2013, *Monthly Notices of the Royal Astronomical Society*, 434, L46, doi: [10.1093/mnras/slt074](https://doi.org/10.1093/mnras/slt074)
- Wang, J., Santos, M. G., Bull, P., et al. 2021, *Monthly Notices of the Royal Astronomical Society*, 505, 3698, doi: [10.1093/mnras/stab1365](https://doi.org/10.1093/mnras/stab1365)
- Wolz, L., Abdalla, F. B., Alonso, D., et al. 2015, in *Advancing Astrophysics with the Square Kilometre Array (AASKA14)*, 35, doi: [10.22323/1.215.0035](https://doi.org/10.22323/1.215.0035)
- Wolz, L., Blake, C., Abdalla, F. B., et al. 2017, *Monthly Notices of the Royal Astronomical Society*, 464, 4938, doi: [10.1093/mnras/stw2556](https://doi.org/10.1093/mnras/stw2556)
- Wolz, L., Pourtsidou, A., Masui, K. W., et al. 2022, *Monthly Notices of the Royal Astronomical Society*, 510, 3495, doi: [10.1093/mnras/stab3621](https://doi.org/10.1093/mnras/stab3621)
- Wu, F., Li, J., Zuo, S., et al. 2021, *Monthly Notices of the Royal Astronomical Society*, 506, 3455, doi: [10.1093/mnras/stab1802](https://doi.org/10.1093/mnras/stab1802)
- Wu, P.-J., Li, Y., Zhang, J.-F., & Zhang, X. 2023a, *Science China Physics, Mechanics, and Astronomy*, 66, 270413, doi: [10.1007/s11433-022-2104-7](https://doi.org/10.1007/s11433-022-2104-7)
- Wu, P.-J., Shao, Y., Jin, S.-J., & Zhang, X. 2023b, *Journal of Cosmology and Astroparticle Physics*, 2023, 052, doi: [10.1088/1475-7516/2023/06/052](https://doi.org/10.1088/1475-7516/2023/06/052)
- Wu, P.-J., & Zhang, X. 2022, *JCAP*, 01, 060, doi: [10.1088/1475-7516/2022/01/060](https://doi.org/10.1088/1475-7516/2022/01/060)
- Wyithe, J. S. B., & Loeb, A. 2008, *Monthly Notices of the Royal Astronomical Society*, 383, 606, doi: [10.1111/j.1365-2966.2007.12568.x](https://doi.org/10.1111/j.1365-2966.2007.12568.x)
- Wyithe, J. S. B., Loeb, A., & Geil, P. M. 2008, *Monthly Notices of the Royal Astronomical Society*, 383, 1195, doi: [10.1111/j.1365-2966.2007.12631.x](https://doi.org/10.1111/j.1365-2966.2007.12631.x)
- Xu, Y., Wang, X., & Chen, X. 2015, *The Astrophysical Journal*, 798, 40, doi: [10.1088/0004-637X/798/1/40](https://doi.org/10.1088/0004-637X/798/1/40)
- Zernike, F. 1934, *Monthly Notices of the Royal Astronomical Society*, 94, 377, doi: [10.1093/mnras/94.5.377](https://doi.org/10.1093/mnras/94.5.377)
- Zhang, J., Liu, J., Wu, F., et al. 2021, *IEEE Antennas and Propagation Magazine*, 63, 98, doi: [10.1109/MAP.2021.3115757](https://doi.org/10.1109/MAP.2021.3115757)
- Zhang, M., Li, Y., Zhang, J.-F., & Zhang, X. 2023, *Monthly Notices of the Royal Astronomical Society*, 524, 2420, doi: [10.1093/mnras/stad2033](https://doi.org/10.1093/mnras/stad2033)
- Zhang, M., Wang, B., Wu, P.-J., et al. 2021, *Astrophys. J.*, 918, 56, doi: [10.3847/1538-4357/ac0ef5](https://doi.org/10.3847/1538-4357/ac0ef5)